Available online at www.sciencedirect.com
ScienceDirect
Trans. Nonferrous Met. Soc. China 34(2024) 977−994
Transactions of Nonferrous Metals Society of China
www.tnmsc.cn

# Damage evolution and destabilization precursors in granite under splitting load at different temperatures

Li-chang WANG[1,2], Lu WANG[1,2], Meng XU[1,2], Wei LONG[1,2]

1. School of Geosciences and Info-Physics, Central South University, Changsha 410083, China;
2. Key Laboratory of Metallogenic Prediction of Nonferrous Metals and Geological Environment Monitoring of Ministry of Education, Central South University, Changsha 410083, China

Received 5 February 2023; accepted 9 November 2023

**Abstract:** Brazilian splitting acoustic emission (AE) tests were conducted on the granite specimens that were heated at the temperatures from 50 to 600 °C to investigate the mechanical and damage characteristics of granite under high temperatures and splitting load in deep drilling. The results indicate that temperature variations significantly alter the mechanical characteristics and AE properties of granite, thereby influencing the evolution of fractures. At the temperature above 500 °C, the tensile strength of granite decreases significantly and the proportion of shear-induced damage modes increases. Furthermore, the rate of fracturing also exhibits a noticeable increase. Damage parameter mutation points on the damage parameter evolution curves of hit counts and energy counts were defined to determine the rock damage precursor. Mutation points based on hit counts arrive earlier than rock instability signals. The greater the damage is, the earlier the mutation points arrive. This time difference can be used to identify rock destabilization signals.
**Key words:** deep drilling; rock damage; acoustic emission; high temperature; splitting load

## 1 Introduction

Deep earth drilling is crucial for understanding deep earth structure, evolutionary processes relevant to life, and exploring deep-seated resources [1−3]. As drilling depths increase, subsurface temperatures rise, negatively influencing deep-seated rock formations and leading to changes in their physical and mechanical attributes. These changes render deep rocks unstable, impeding drilling and posing risks of engineering disasters [4,5]. Therefore, investigating the tensile properties, damage evolution, and failure modes of rocks under high-temperature conditions is important [6,7].

As temperatures rise, granite formations develop defects that lead to damage. The mineral composition and crystal phase of granite undergo changes, forming micro-cracks that reduce its tensile strength [8−10]. Empirical investigations by SHA et al [11] and GAO et al [12] have identified 400 °C as a pivotal temperature threshold marking a substantial diminution in the tensile strength of granite, with a pronounced decline manifesting at 573 °C. Furthermore, studies conducted by WU et al [13] have elucidated that temperatures exceeding 500 °C lead to a rapid escalation in the porosity of granite. Additionally, ZHAO et al [14] and YIN et al [15] reported that temperature affects the quantity and type of microcracks in granite, leading to a deterioration in its physical and mechanical properties. Understanding the relationship between tensile strength and internal damage in granite is important for comprehending its failure mechanisms. LIANG et al [16] established a

**Corresponding author:** Meng XU, Tel: +86-13975809372, E-mail: xumeng@csu.edu.cn
DOI: 10.1016/S1003-6326(23)66447-7

quantitative relation between tensile strength and internal damage in granite across temperatures, utilizing wave velocity as an indicator. However, these investigations have not fully correlated the mechanical characteristics of rocks with the damage evolution process or effectively identified the precursor information on rock fracture and the internal rupture modes.

Acoustic emission (AE) technology represents a powerful tool for addressing the aforementioned issues. AE technology was developed in the 1960s, and it has been widely adopted for monitoring and assessing rock damage progression since then. As internal fractures develop, strain energy is released, rapidly emitting elastic waves, known as AE events [17,18]. This connection between AE events and fracture extension allows for real-time monitoring of acoustic signals related to internal rock rupture and damage development [19,20]. A myriad of parameters derived from AE signals can be harnessed to elucidate the damage evolution within rocks, including but not limited to peak frequency, rise time/amplitude (RA), average frequency (AF), AE ring counts, and energy. Notably, during rock splitting failures, peak frequency signals in AE exhibit correlations with the scale of fractures, with smaller fractures being associated with higher peak frequencies [21]. Furthermore, low-frequency signals tend to exhibit greater frequency and carry more substantial energy in comparison to their high-frequency counterparts [22]. The RA and AF values can be used to determine the dominant fracture modes, such as the tensile damage during Brazilian splitting [23,24]. Different damage variables can be obtained by analyzing the AE ringing counts and energy counts. The variables are used to understand the relationship between mechanical properties and damage development, allowing the formulation of equations that capture the evolution of rock damage and its impact on deformation properties. The interplay between the mechanical properties of rocks and damage development can be further elucidated through the analysis of different damage variables derived from AE ring counts and energy counts, thereby enabling the formulation of equations that encapsulate rock damage evolution and its consequent impact on deformation properties [25]. Moreover, the AE parameters allow for the identification of precursors indicating rock instability. For instance, ZHANG et al [26] found that high ring counts, protracted durations, and elevated energies can indicate impending rock instability.

In our investigation, we employed AE technology to study the relationship between mechanical characteristics and damage evolution of granite subjected to splitting loads at different temperatures. We analyzed damage variables and identified mutation points in the damage parameter derived from AE signals, which help us deeply understand the precursors that indicate granite destabilization. This approach can enhance the safety and efficacy of deep earth drilling operations.

## 2 Experimental

### 2.1 Specimen preparation

The granite specimens used in this study were sourced from formations within the Dingziwan region, located in the Wangcheng−Zhuzhou Fracture Zone (F Xiang-00030). Characterized by a grayish-white color, these specimens possess a massive structure with a medium-coarse grain texture. Mineralogically, the specimens are composed predominantly of alkaline feldspar (approximately 41 wt.%), followed by intermediate-acid plagioclase (approximately 26 wt.%), and quartz (approximately 27 wt.%). Secondary minerals include muscovite and biotite, comprising about 5 wt.% and 1 wt.%, respectively, as illustrated in Fig. 1. The size of the mineral particles in these specimens ranges from 0.5 to 2.5 mm.

Preparatory to conducting the test procedures, the samples were meticulously fashioned into disc-

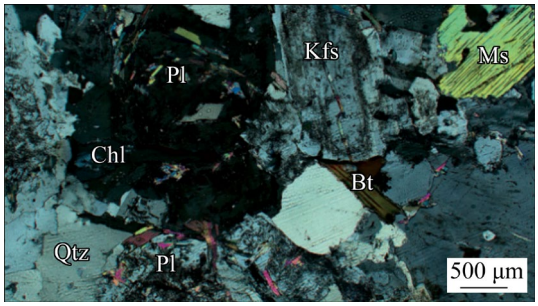


**Fig. 1** Microscopic mineral composition of granite (Qtz−Quartz; Chl−Chlorite; Pl−Plagioclase; Kfs−K-feldspar; Bt−Biotite; Ms−Muscovite)

shaped specimens, following the international standard for rock mechanics, with each disc possessing a diameter of 50 mm and a height of 25 mm.

### 2.2 Heat treatment of specimens

Prior to heating, the seven samples were pre-treated to remove surface moisture. This involved a drying process at 50 °C for 24 h, which for the purposes of this study, is defined as room temperature. The specimen surfaces were then finely polished to achieve uniformity.

Following this preparation, the samples were heated in a muffle furnace at a rate of 5 °C/min to target temperatures of 100, 200, 300, 400, 500, and 600 °C. After reaching each target temperature, the samples were maintained at a constant temperature for 3 h before the furnace was turned off, allowing them to cool naturally to room temperature. Once cooled, each sample was carefully retrieved, labeled, and a uniform layer of white paint was applied to their bases to aid in further morphological analyses. Notably, the samples did not exhibit visible fractures on their surfaces up to the maximum temperature of 600 °C, as illustrated in Fig. 2.

### 2.3 Tensile strength mechanical test program and parameter setting

The Brazilian splitting test was executed on the specimens utilizing the YDW−100 rock-splitting testing machine. The loading protocol was displacement-controlled, administered by a hydraulic press machine, operating at a controlled loading rate of 0.05 mm/min. For the concurrent AE data collection, a DS5 series Full Information AE signal analyzer, manufactured by Beijing Softland Times Science & Technology Co., Ltd, was employed. Two RS−5A sensors were meticulously positioned diagonally across the two opposing end faces of each specimen. These sensors boasted a frequency range spanning 50 to 800 kHz. Specific parameter configurations included a detection threshold set at 40 dB, a sampling frequency of 3 MHz, a resonance frequency of 225 kHz, and a sampling length of 5 kb.

To facilitate consistent AE signal acquisition while mitigating the risk of sensor dislodgement during the loading process, Vaseline was judiciously selected as the coupling agent. Additionally, insulating tape was judiciously applied to securely affixing the sensors to the specimen. The detailed test arrangement, sensor installation method, and precise sensor placement are visually elucidated in Fig. 3.

It is imperative to underscore that throughout the testing regimen, meticulous synchronization between the rock mechanics test system and the AE monitoring system was diligently upheld. This synchronization served to ensure the precise temporal alignment of mechanical data acquisition and AE data capture, thus contributing to the reliability and coherence of the experimental data set.

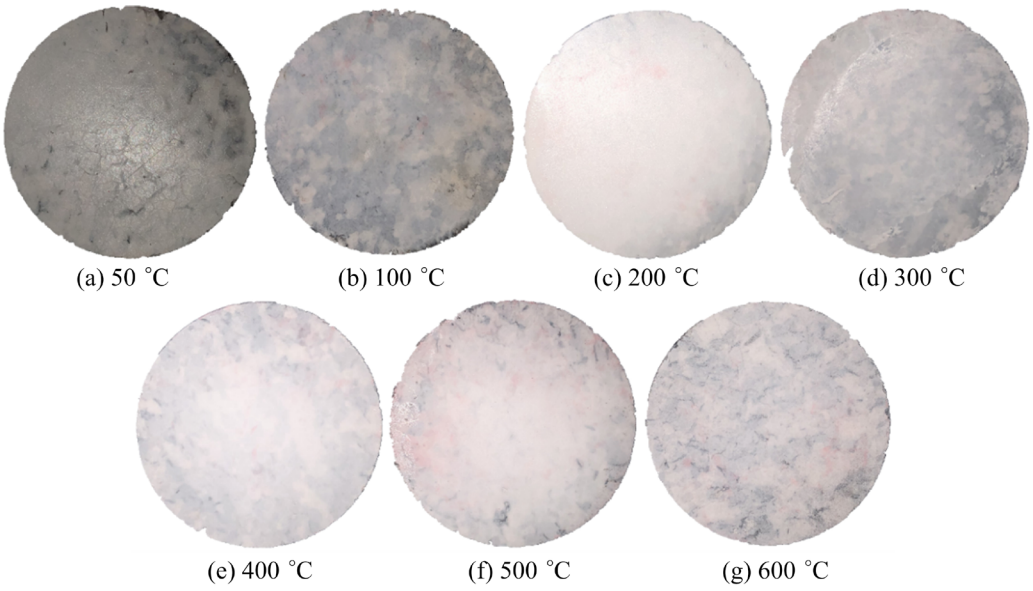


**Fig. 2** Surface morphology of granite after heating at different temperatures

## 3 Results and discussion

### 3.1 Brazilian splitting morphology and tensile strength analysis of granite

In the course of the Brazilian splitting test, the specimen underwent cleavage, effectively separating into two distinct fragments along the loading direction, originating from the point of contact between the upper and lower wire gaskets. Subsequent to this fracture event, the broken sections, upon being juxtaposed, revealed the presence of a conspicuous through crack centrally positioned within the specimen. The morphological depiction of this damage manifestation is presented in Fig. 4.

Observations gleaned from this experimental framework indicate that an escalation in the target temperature yields a corresponding augmentation in the extent of cracks and debris near the fracture plane. Concomitantly, the stress level requisite for triggering splitting failure exhibits a progressive diminishment, and the sound emitted during the damage process evolves from being sonorously crisp to markedly subdued.

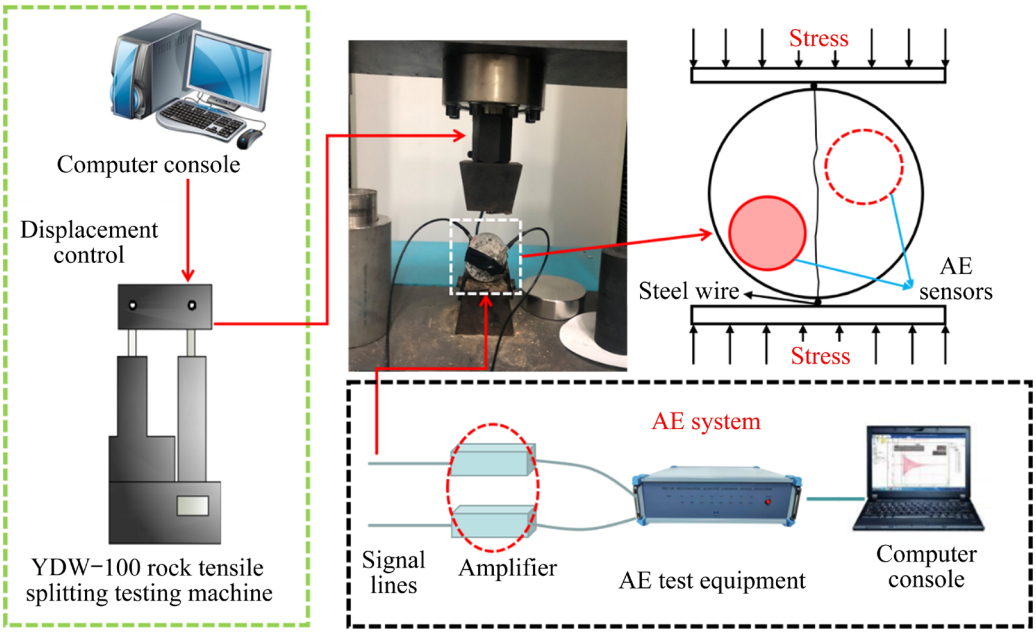


**Fig. 3** Overall test arrangement and installation method and location of AE sensors

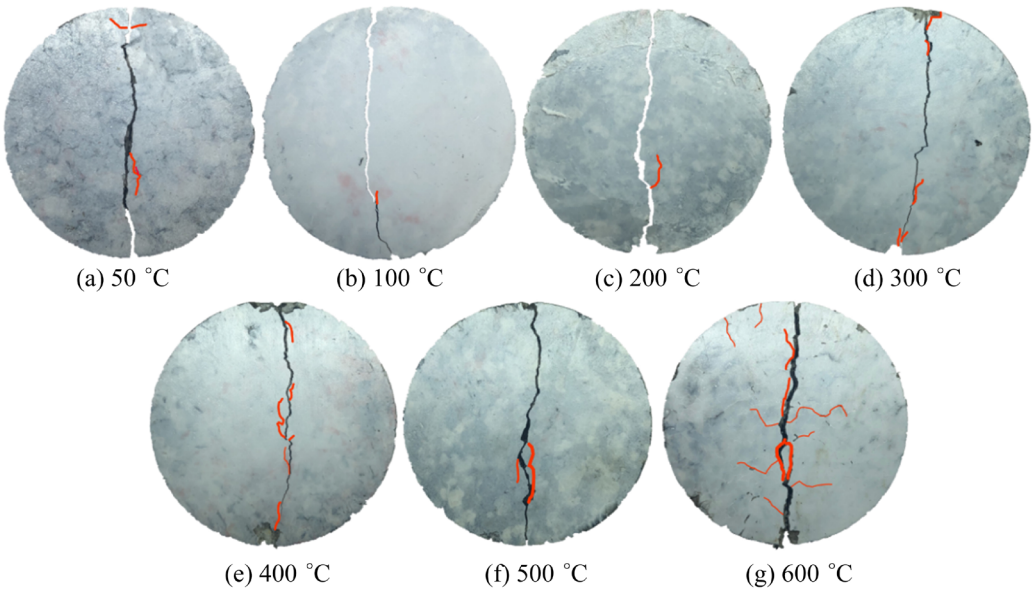


**Fig. 4** Surface morphology of granite after splitting at different temperatures

From a macroscopic perspective concerning mechanical properties, it becomes evident that the tensile strength of granite experiences a progressive decline with increasing temperature, primarily attributable to thermal-induced damage phenomena. This decline is notably discernible within the temperature range of 200−300 °C, during which the expulsion of strongly bound water occurs. Moreover, crystallization water precipitates from the rock matrix at approximately 400 °C. These thermal processes precipitate a deleterious impact on the microstructural integrity of mineral constituents and subsequently attenuate inter-mineral bonding [27].

Simultaneously, the expansion of mineral particles due to thermal effects engenders structural thermal stress effects. This leads to the manifestation of grain boundary fractures, intragranular cracks, or transcrystalline fractures within the rock matrix, resulting in the disruption of its originally intact structure and the consequent impairment of the rock's structural integrity. Furthermore, temperatures exceeding 573 °C induce a transformation in the quartz minerals present in granite, transitioning them from the $\alpha$ to $\beta$ phase, causing certain fragments to detach from the specimen [28,29].

Moreover, it is noteworthy that at temperatures lower than 400 °C, internal crystallization within the specimen provokes the closure of certain primary microfractures. Conversely, temperatures exceeding 400 °C prompt an intensification of high-temperature mineral crystal expansion, thereby amplifying damage within the specimen. Consequently, specimens subjected to treatment at 600 °C exhibit a heightened degree of damage and a precipitous drop in tensile strength. Interestingly, the microfractures within the specimens display an initial reduction followed by an increment in density as the temperature escalates.

The numerical values reflecting the tensile strength of granite specimens at each designated temperature are presented in Table 1. Notably, there is a decrease in tensile strength from 7.68 to 6.09 MPa, representing a 20.7% reduction when the temperature is elevated from 50 to 200 °C. Subsequently, from 200 to 300 °C, the tensile strength experiences a further decline, decreasing by 25.8% from 6.09 to 4.52 MPa. This substantial decrease in tensile strength during this interval is primarily attributed to damage ensuing from the release of tightly bound water and gases within the specimen, in conjunction with the influence of structural thermal stress.

**Table 1** Tensile strength of granite at each temperature

| Heating temperature/°C | Tensile strength/MPa |
|---|---|
| 50 | 7.68 |
| 100 | 4.7 |
| 200 | 6.09 |
| 300 | 4.52 |
| 400 | 4.29 |
| 500 | 4.25 |
| 600 | 2.62 |

Comparatively, the alteration in tensile strength is less pronounced for specimens subjected to temperatures of 400 and 500 °C, with the tensile strength of the former exhibiting a mere 5.1% reduction relative to the 300 °C specimens, and the latter recording a marginal 0.9% decrease in relation to the 400 °C specimens. The reduction in tensile strength is mitigated during this phase, as the thermal expansion of mineral particles results in the closure of primary microcracks through extrusion. Consequently, the decline in tensile strength is moderated and, in certain instances, may even exhibit an increase.

The final stage, wherein temperatures ascend from 500 to 600 °C, witnesses a substantial drop in tensile strength. Specifically, the tensile strengths plummet from 4.25 to 2.62 MPa, representing a dramatic 38.4% reduction. During this period, the transformation of quartz phases engenders a significant deterioration in the tensile strength of specimens treated at 600 °C.

### 3.2 Analysis of Brazilian splitting process of granite

The stress−time curves of granite subjected to varying elevated temperatures under Brazilian splitting conditions were ascertained in the course of this investigation, as illustrated in Fig. 5.

The stress evolution within the specimen can be demarcated into three discernible stages.

(1) Compaction phase: The initial stage is characterized as the compaction phase. As the indenter descends following the application of load,

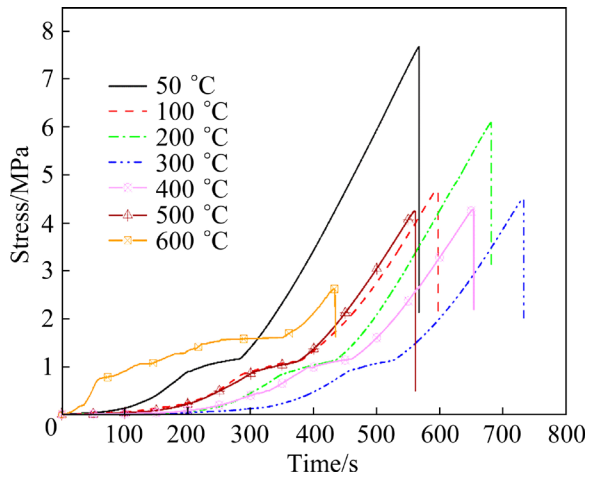


**Fig. 5** Time−stress curves of Brazilian splitting of granite at different temperatures

stress incrementally ascends, exhibiting a discernible up-concave trajectory. During this phase, stress generation commences at the interface between the steel wire spacer and the specimen, leading to localized deformation and stress concentration at the point of contact. Concurrently, primary microcracks within the specimen gradually diminish as the indenter displacement increases.

(2) Linear elastic regime: Subsequent to the compaction phase, the stress enters a linear elastic stage. Upon the conclusion of the microcrack compaction phase, stress exhibits a rapid and linear growth pattern. This phase is marked by the emergence of numerous new cracks within the specimen, which proceed to propagate.

(3) Failure instability phase: The final stage is characterized as the failure instability phase. This stage typically encompasses the interval where stress levels approach 90% of the peak strength. Notably, stress within this stage continues to exhibit linear growth, indicative of pronounced brittle damage.

### 3.3 AE frequency characteristics under splitting load

Internal and external loads cumulatively store energy within rocks through deformation processes. Subsequent rock damage and failure events release this stored strain energy in the form of elastic stress waves, thereby giving rise to the phenomenon of AE [30−32]. Consequently, AE signals emanating from rocks during testing serve as indicators of microcrack development within the rock matrix.

The peak frequency of AE signifies the frequency at which the energy spectrum reaches its maximum point. This peak frequency can be approximated as the principal frequency of the signal and categorized into two main groups: low-frequency signals (ranging from 100 to 200 kHz) and high-frequency signals (exceeding 350 kHz). The utilization of peak frequency facilitates the assessment of microcrack expansion within rocks [33,34], with higher signal frequencies correlating with smaller rupture source scales. In indoor rock rupture AE signals, frequencies typically exceed 100 kHz, while signals between 350 and 500 kHz are infrequent. This phenomenon can be attributed to the inverse relationship between the frequency of the signal and the scale of the rupture source. Rupture sources of a small scale generate signals characterised by high frequency and low energy. The detection of such signals is impeded by the phenomenon of attenuation and the thresholds set by the AE system. Consequently, special attention should be directed toward signals exceeding 350 kHz due to the abundance of small-scale fracture signals originating from the controlled fractures encountered in the Brazilian splitting tests.

Figure 6 graphically depicts the correlation between peak AE frequency and stress over time under various temperature conditions during Brazilian splitting tests. In this illustration, Regions I, II and III correspond to the compaction stage, linear elastic stage, and failure destabilization stage, respectively.

During the compaction stage, the generation of low-frequency signals can generally be attributed to the closure of microfractures or joint surfaces within the rock, as well as the sliding of the specimen during compression. At the linear elastic stage, the emergence of low-frequency signals is linked to the formation, propagation, and transfixion of microfractures within the rock, exacerbating its structural damage and giving rise to an increased prevalence of shear failure modes. Consequently, a substantial number of low-frequency signals are produced. Conversely, the presence of high-frequency signals signifies the development of small-scale cracks. Table 2 provides a breakdown of the proportion of low-frequency to high-frequency signals for each test specimen at different testing stages.

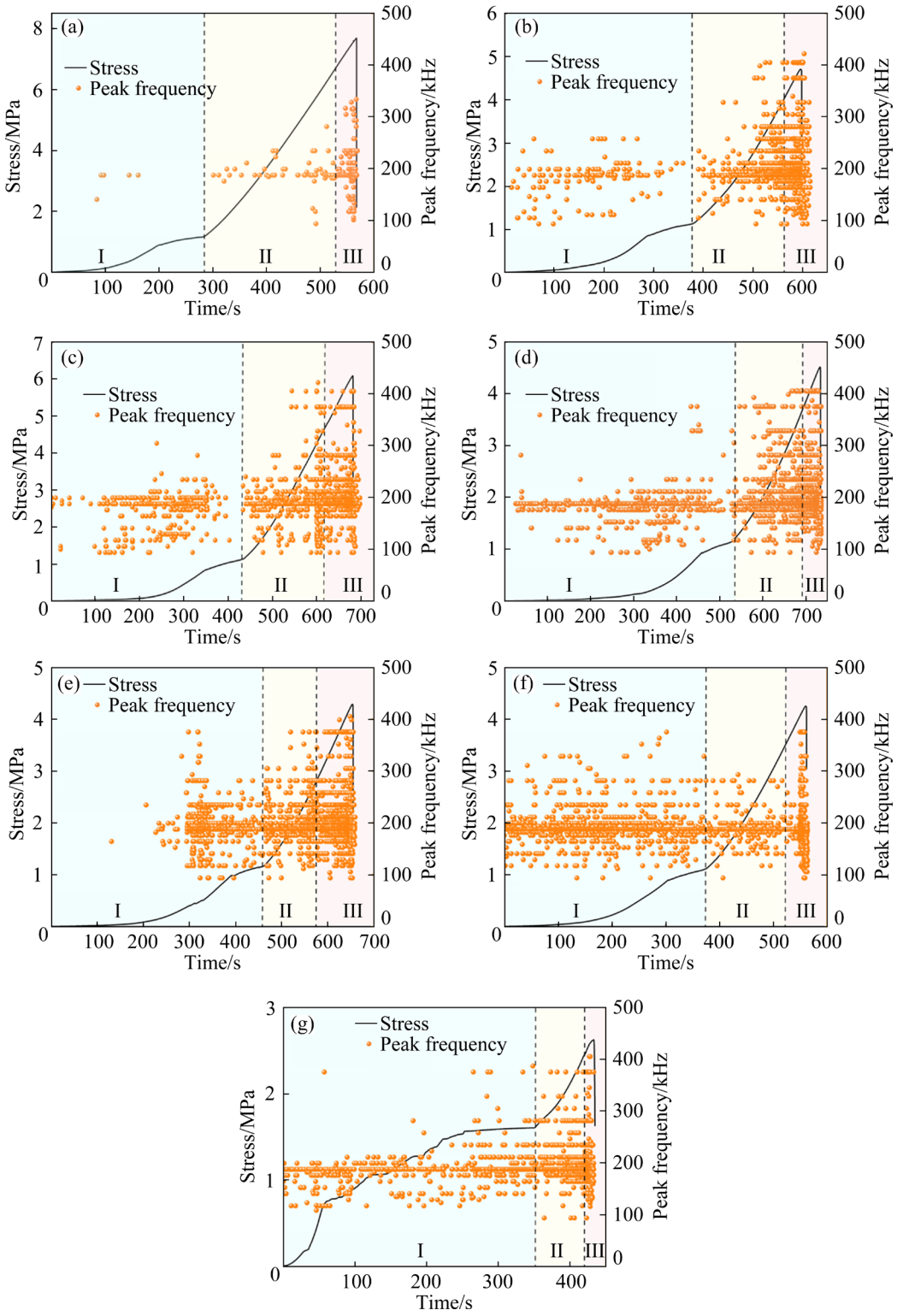


**Fig. 6** Trend of stress and peak AE frequency with time for granite under splitting load at different temperatures: (a) 50 °C; (b) 100 °C; (c) 200 °C; (d) 300 °C; (e) 400 °C; (f) 500 °C; (g) 600 °C

For specimens subjected to temperatures between 50 and 400 °C, their peak frequencies during the compaction stage all fall within the low-frequency signal range. During the later stages of the linear elastic phase, there is a significant increase in low-frequency signals, accompanied by the appearance of a greater number of high-frequency signals. This observation suggests that exposure to temperatures between 50 and 400 °C facilitates the development, accumulation, and

**Table 2** Proportion of low-frequency signals (100− 200 kHz) and high-frequency signals (above 350 kHz) of granite at compaction stage, linear elastic stage, and failure destabilization stage at different temperatures

| Heating temperature/°C | Proportion of low-frequency signal/% | | | Proportion of high-frequency signal/% | | |
|---|---|---|---|---|---|---|
| | Compaction stage | Linear elastic stage | Failure destabilization stage | Compaction stage | Linear elastic stage | Failure destabilization stage |
| 50 | 100.0 | 82.5 | 76.3 | 0.0 | 0.0 | 0.0 |
| 100 | 37.5 | 51.4 | 60.4 | 0.0 | 0.8 | 5.4 |
| 200 | 89.3 | 77.1 | 77.5 | 0.0 | 2.3 | 2.7 |
| 300 | 89.9 | 66.6 | 75.7 | 0.0 | 5.1 | 4.8 |
| 400 | 72.9 | 71.9 | 75.1 | 0.6 | 2.7 | 3.5 |
| 500 | 85.3 | 87.9 | 90.7 | 0.4 | 0.0 | 1.6 |
| 600 | 90.6 | 78.7 | 85.9 | 0.7 | 0.8 | 2.1 |

penetration of internal microfractures within the granite specimens, ultimately resulting in the formation of larger-scale cracks that contribute to specimen damage.

In contrast, specimens exposed to temperatures of 500 and 600 °C generate a higher number of low-frequency signals during the compaction stage, with a limited presence of high-frequency signals at this point. Subsequently, at the linear elastic stage, both low and high-frequency signals increase in number and reach their peak levels at the time of failure. This pattern indicates that temperatures exceeding 500 °C intensify internal damage within the granite specimens. Such elevated temperatures induce a greater number of fractures throughout all phases of testing, with fractures expanding more rapidly, ultimately leading to the accelerated destruction of the granite specimens. These findings are congruent with the concurrent results indicating lower tensile strength under such conditions.

### 3.4 Analysis of failure modes based on AE

The combination of RA and AF values is a common approach utilized in rock mechanics to assess whether rock failure occurs under tensile or shear conditions [35]. In the context of AE analysis, the RA value represents the reciprocal of the gradient of the signal waveform and can be computed by dividing the rise time by the signal's amplitude within the AE parameter framework. On the other hand, the AF value denotes the ratio between AE ring counts and the duration, representing the average frequency of AE events. When these values are plotted in the RA−AF distribution, a discernible diagonal line emerges, serving as a criterion for distinguishing between tensile and shear failure modes (JCMS-III b5706, 2003). Specifically, regions above and below this dividing line correspond to tensile and shear failure intervals, respectively [36]. Notably, transitions in AF values from high to low are indicative of the progressive development of larger cracks [37].

Figure 7 illustrates the distribution of RA and AF values of granite specimens at different stages of compaction process, encompassing the compaction stage, linear elastic stage, and failure destabilization stage, all subjected to temperature treatment ranging from 50 to 600 °C. To complement this analysis, Tables 3 and 4 provide comprehensive data regarding the distribution frequencies of AE signals for each specimen, along with the corresponding percentages of signals located within the shear failure region, across the various testing stages, namely the compaction stage, linear elastic stage, and failure destabilization stage.

Granite specimens subjected to varying temperature treatments consistently exhibited a noteworthy pattern characterized by elevated AF values and diminished RA values. A substantial concentration of data points was observed within the tensile failure region, closely aligned with the longitudinal axis. In contrast, a comparably sparse distribution of data points was evident within the shear failure interval, predominantly manifesting during the failure destabilization stage. Within the context of Brazilian splitting tests, it was evident that tensile cracking constituted the dominant fracture mode within the granite specimens, whereas shear cracking played a sub-dominant role. Remarkably, this fracture pattern remained unaltered across the spectrum of temperatures tested, suggesting that the prevailing mechanical loading

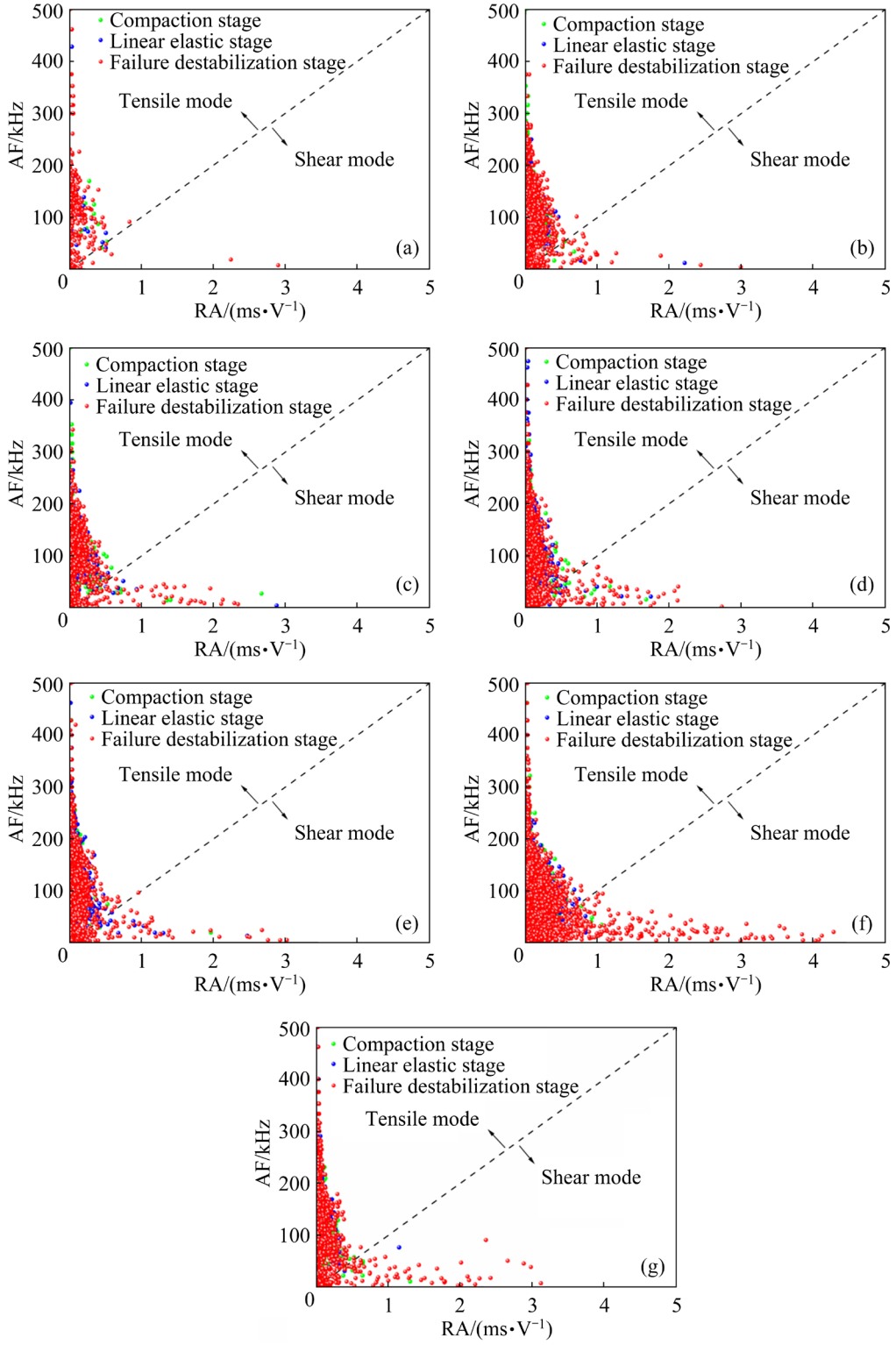


**Fig. 7** Distribution of RA and AF values in AE signal of granite under splitting load at different temperatures: (a) 50 °C; (b) 100 °C; (c) 200 °C; (d) 300 °C; (e) 400 °C; (f) 500 °C; (g) 600 °C

conditions exerted a more profound influence on fracture mode determination, rather than structural alteration.

Intriguingly, Table 3 revealed a gradual escalation in the percentage of shear cracking occurrences with rising temperatures, with the bulk of shear failures becoming prominent near the threshold of peak stress intensity. Notably, within the realm of acoustic emission analysis, high-frequency signals typically signify the initiation of

**Table 3** Proportion of granite AE signal at compaction stage, linear elastic stage, and failure destabilization stage at different temperatures

| Heating temperature/°C | Distribution proportion/% | | |
|---|---|---|---|
| | Compaction stage | Linear elastic stage | Failure destabilization stage |
| 50 | 5.08 | 8.13 | 86.79 |
| 100 | 12.1 | 9.86 | 78.04 |
| 200 | 21.02 | 21.09 | 57.89 |
| 300 | 19.37 | 32.77 | 47.86 |
| 400 | 11.71 | 31.92 | 56.37 |
| 500 | 13.22 | 13.64 | 73.14 |
| 600 | 15.32 | 15.67 | 69.01 |

**Table 4** Proportion of granite AE signals in shear mode at compaction stage, linear elastic stage, and failure destabilization stage at different temperatures identified by RA−AF distribution

| Heating temperature/°C | Proportion located in shear mode/% | | |
|---|---|---|---|
| | Compaction stage | Linear elastic stage | Failure destabilization stage |
| 50 | 0.23 | 0.46 | 1.54 |
| 100 | 1.85 | 1.94 | 0.33 |
| 200 | 2.25 | 1.89 | 5.39 |
| 300 | 1.63 | 1.22 | 6.29 |
| 400 | 0.96 | 1.41 | 3.78 |
| 500 | 0.69 | 1.73 | 10.98 |
| 600 | 1.69 | 0.55 | 6.52 |

small fractures, while low-frequency signals are indicative of the emergence of larger fractures. High-frequency signals are characterized by abbreviated rise time, shorter duration, heightened amplitudes, and a greater number of AE ring counts, whereas low-frequency signals exhibit contrasting characteristics. Consequently, high-frequency signals manifest lower RA and elevated AF when compared to their low-frequency counterparts.

Consequently, the analytical findings outlined in Section 3.3 elucidate that as the treatment temperature escalates, there is a discernible augmentation in the proportion of low-frequency signals, thereby yielding an expanded dataset characterized by high RA and diminished AF. This substantiates the assertion that the proportion of shear damage mode within the granite amplifies concomitantly with the escalating treatment temperature during the process of splitting failure.

It is worth noting that an increasing prevalence of the shear damage mode during the rock's failure process corresponds to a more pronounced internal damage evolution within the rock matrix [24]. This corroborates the assertion that the internal damage within the granite specimen experiences progressive intensification with the increasing treatment temperature.

### 3.5 Analysis of damage evolution of granite

#### 3.5.1 Ring count characteristics of granite splitting failure

AE ring counts refer to the quantification of oscillations exhibited by the ringing pulse as it surpasses the threshold signal within a unit of time. This metric exhibits heightened sensitivity to the deformation and structural degradation of rock specimens and, consequently, serves as an indicator of damage accumulation throughout the course of rock splitting failures [38]. It is important to note that an elevated ring count corresponds to a greater degree of internal damage within the rock under equivalent conditions [39]. To visualize these dynamics, Fig. 8 presents time-dependent profiles encompassing load variation, AE ring count, and cumulative energy during the Brazilian splitting tests conducted on granite specimens subjected to diverse heat treatment temperatures.

To enhance the clarity of trends within the graphical representation, the axes corresponding to ring counts and cumulative energy have been adjusted non-linearly. Notably, the following observations can be derived from the figure.

(1) In the temperature range of 50−400 °C, the AE signals exhibit relatively low quantities and diminished intensities, with AE ring counts rarely exceeding 100. During the compaction stage, the occurrence of both ring counts and energy signals is limited and fragmented. As loading progresses into the linear elastic stage, there is a discernible breakdown in the connection among mineral particles, leading to the expansion of primary cracks, the emergence of secondary cracks, and the gradual convergence of these fissures. Consequently, the extent of rock damage steadily increases, thereby resulting in a corresponding augmentation

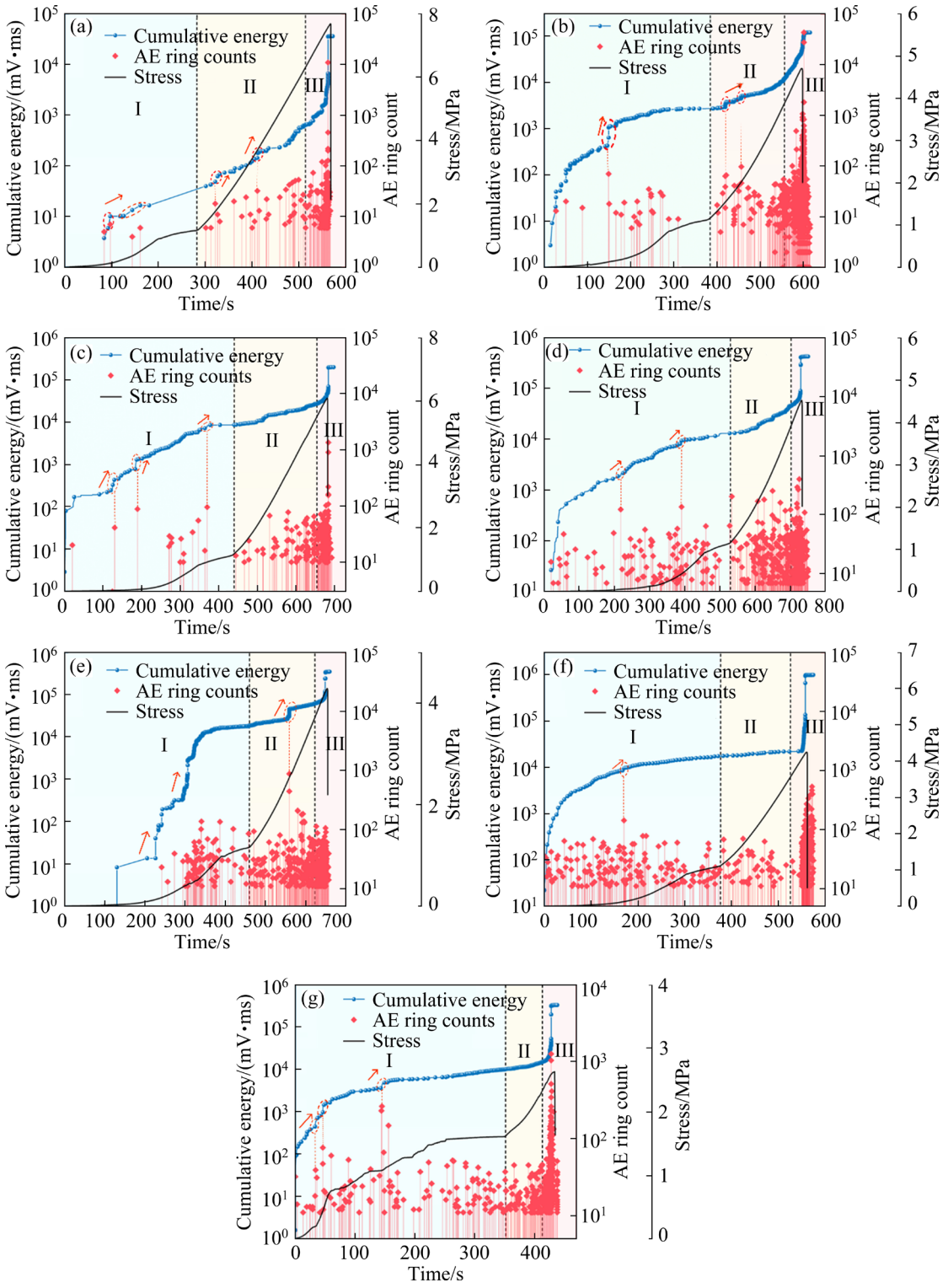


**Fig. 8** Variation of AE ring count, cumulative energy, and stress with time for granite under splitting load at different temperatures: (a) 50 °C; (b) 100 °C; (c) 200 °C; (d) 300 °C; (e) 400 °C; (f) 500 °C; (g) 600 °C

of AE signals. Throughout the failure destabilization stage, the internal fractures within the granite rapidly propagate and expand, culminating in an intensive surge in signal occurrence, particularly exemplified by a rapid escalation in AE ring counts near the peak stress intensity. These observations collectively indicate that thermal damage within the rock is relatively subdued within this temperature range. Specifically, during the compaction stage, internal damage

exhibits limited development under lower stress conditions. However, as higher stresses are encountered upon transitioning into the linear elastic stage, damage progression becomes more pronounced. Ultimately, during the failure destabilization stage, damage accelerates to attain its zenith, accompanied by an instantaneous release of a substantial amount of energy, leading to the catastrophic failure of the specimen. It is evident that, within this temperature interval, the observed AE signal trends consistently underscore the incremental thermal damage within the granite as temperatures rise.

(2) Conversely, at heating temperatures of 500 and 600 °C, AE signals are distributed densely throughout the entire loading process, characterized by the pervasive occurrence of high-intensity AE ring count signals. This conspicuous pattern signifies that thermal damage beyond the threshold of 500 °C leads to a rapid deterioration in the mechanical properties of granite specimens.

3.5.2 Energy evolution characteristics of granite splitting failure

Among the suite of AE parameters, the parameter known as “energy” assumes a pivotal role as it provides a measure of the relative energy or intensity released during an AE event. Notably, the magnitude of this energy can be viewed as a direct reflection of the scale of crack formation within the rock. Consequently, it serves as a vital indicator for characterizing the failure of the internal microstructure of the rock [40]. To facilitate the interpretation of key trends, Fig. 8 portrays the temporal evolution of cumulative energy, ring counts, and stress, with the axes pertaining to cumulative energy and ring counts subjected to logarithmic scaling for enhanced visualization.

Within the schematic representation, Regions I, II and III distinctly demarcate the compaction stage, linear elastic stage, and failure destabilization stage, respectively. During the compaction stage, the frequency of energy signals is relatively sparse, and the overall magnitude of released energy remains modest. This observed phenomenon is attributed to the inadequacy of the applied load at this stage to disrupt the internal cohesion, primary pore networks, and pre-existing cracks within the granite specimen. Furthermore, the load conditions are insufficient to generate new microcracks. Consequently, the majority of the energy imparted by the applied load accumulates internally within the specimen, with only a fraction being liberated to generate discernible energy signals.

It is in the transitional phase spanning from the linear elastic stage to the failure destabilization stage that a notable escalation in energy signals is observed, accompanied by a significant amplification in the overall level of energy release. This shift in energy dynamics aligns with the progressive development of rock damage and the concurrent formation of fractures.

The assessment of crack formation size is facilitated by amalgamating temporal patterns in accumulated energy, ring counts, and stress variations. For instance, instances where cumulative energy data exhibit a rapid upswing, concomitant with the generation of elevated ring count signals, indicate the initiation of larger-scale fractures within the granite. Additionally, as the specimen approaches its upper limit tensile strength, a synchronized surge in both accumulated energy and ring counts to a higher order of magnitude serves as a conspicuous indicator that the rock’s damage threshold has been reached, and the specimen is poised for destabilization. This coalescence of increased energy and ring counts signifies the culmination of damage progression within the rock and heralds the imminent failure of the specimen.

3.5.3 Damage evolution characteristics of granite splitting failure

Under the influence of stress, continuous damage unfolds within the rock mass, ultimately culminating in its structural failure [41]. The AE characteristics exhibited by a material serve as a direct reflection of the ongoing generation and progression of internal damage. Recognizing the intrinsic interplay between damage variables and material structures [42], the Brazilian splitting test provides a viable avenue for scrutinizing the damage processes experienced by high-temperature-treated granite. This, in turn, facilitates the application of damage theory to formulate a comprehensive granite damage model [43].

In this context, the damage variable, $D$, assumes the role of quantifying the state of material degradation. $D$ is established through the division of the cumulative AE ring counts, represented as $C$. It is postulated that the specimen, in its pristine state, possesses no initial damage, signifying $D$=0. The formulation for calculating the damage variable

$D$ is expressed as

$$D=C/C_0 \quad (1)$$

where $D$ signifies the damage variable value of the specimen at the loading time $t$, $C$ represents the cumulative ring counts recorded at the specified loading time $t$, and $C_0$ corresponds to the cumulative AE ring counts observed when the entire section of the nondestructive rock sample undergoes complete failure [44].

By employing Eq. (1), the damage values for individual specimens at each juncture of the splitting process are meticulously computed. Consequently, a comprehensive damage evolution curve encompassing the entire testing procedure is meticulously constructed, as depicted in Fig. 9. It is noteworthy that the damage variable $D$ operates within the range of 0−1, wherein proximity to the value of 1 indicates a higher degree of incurred damage and brings the specimen closer to the threshold of structural failure.

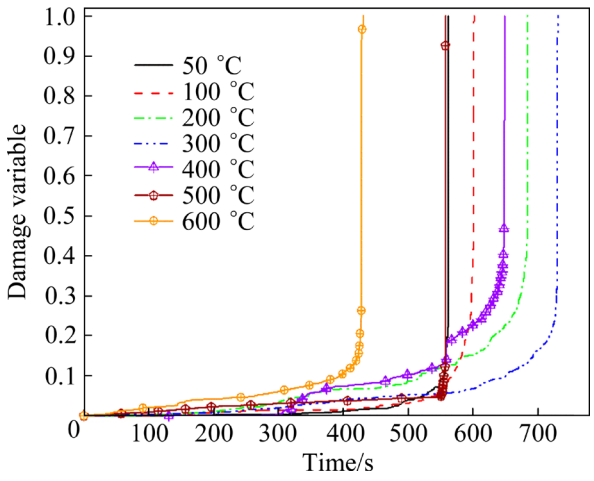


**Fig. 9** Damage evolution curves of granite specimen under splitting load at different temperatures

The damage curve can be delineated into three distinct phases, as depicted in Fig. 9. The initial phase, denoted as the calm phase, exhibits a gentle curve slope, signifying a relatively sluggish growth rate of the damage variable. Subsequently, the second stage, designated as the acceleration stage, is characterized by a notably steeper curve slope, indicative of a rapid escalation in damage progression within a concise timeframe (Table 5). Finally, the third stage, termed as the steep increase period, is typified by an abrupt surge in the damage variable, resulting in its proximity to the critical value of $D$=1. At this juncture, internal fractures have successfully traversed the specimen, precipitating its structural failure and the concomitant release of a substantial energy burst. By fitting all the curves using the exponential to obtain the function $y=a^{bx}$, the damage development proxy $a$ can be obtained. The $a$ values for all specimens are listed in Table 6. The larger the value of $a$, the intenser the damage is.

**Table 5** Slope of granite damage variable vs time curves at second stage

| Heating temperature/°C | Duration/s | $D$ | Slope/$10^{-3}$ |
|---|---|---|---|
| 50 | 73 | 0.07079 | 0.97 |
| 100 | 64 | 0.09182 | 1.44 |
| 200 | 117 | 0.15783 | 1.35 |
| 300 | 107 | 0.10698 | 1.00 |
| 400 | 65 | 0.10491 | 1.61 |
| 500 | 10 | 0.03074 | 3.07 |
| 600 | 18 | 0.03794 | 2.11 |

**Table 6** Values of $a$ in curve-fitting exponential function of granite damage variables

| Heating temperature/°C | $a$/$10^{-4}$ |
|---|---|
| 50 | 0.4 |
| 100 | 4 |
| 200 | 26 |
| 300 | 21 |
| 400 | 11 |
| 500 | 47 |
| 600 | 46 |

In the first stage, damage variables for specimens exposed to temperatures ranging from 50 to 400 °C exhibited negligible growth within the initial 200 s of experimentation. It was only after this duration that damage variables gradually commenced their ascent. Conversely, the curves for specimens subjected to 500 and 600 °C exhibited a sustained, albeit modest, increase in the damage variable from the commencement of testing, signifying the immediate onset of the damage development. During the second stage, at 50−400 °C, the duration extended beyond 60 s. The slope maintained a modest increase, ranging from $0.79\times10^{-3}$ to $1.61\times10^{-3}$. Within this temperature

range, both 100 and 200 °C specimens exhibited similar trends, while the 300 °C specimen experienced a decrease in slope, followed by an ascent to higher levels at 400 °C. This suggests a modest overall increase in damage up to 400 °C, as well as within 100−200 °C. Conversely, at 300 °C, the damage was mitigated due to thermal expansion of internal particles and the closure of microfractures. Notably, upon surpassing 500 °C, the duration of the second stage was substantially shortened to approximately 20 s, accompanied by a significant amplification in slope.

The $a$ values for specimens from 50 to 400 °C remained at a relatively low level throughout the entirety of testing, while those for specimens at 500 and 600 °C displayed a notable increase (see Table 6). This suggests that beyond 500 °C, internal fissures undergo substantial expansion, leading to a significant decrease in specimen strength.

Additionally, AE hit counts and energy counts serve as pivotal indicators of rock damage and play a vital role in damage prediction and early warning [45]. Damage parameters, specifically $D_{\text{hit}}$ and $D_{\text{energy}}$ are computed from AE hit counts and energy counts, respectively, using the following equations:

$$D_{\text{hit}}=E_{t,\text{hit}}/E_{\text{hit}} \tag{2}$$

$$D_{\text{energy}}=E_{t,\text{enerrgy}}/E_{\text{energy}} \tag{3}$$

where $E_{t,\text{hit}}$ and $E_{t,\text{enerrgy}}$ represent the cumulative number of hits and cumulative energy of AE at the stress state at time $t$, while $E_{t,\text{hit}}$ and $E_{t,\text{enerrgy}}$ correspond to the cumulative number and energy of AE impacts of the specimen at peak stress. Specifically, when $E_{t,\text{hit}}$ and $E_{t,\text{enerrgy}}$ assume a value of 0, the specimen remains undamaged, whereas a value of 1 signifies a loss of load−bearing capacity.

The AE hit and energy counts under the splitting load are graphically depicted in Fig. 10.

Both $D_{\text{hit}}$ and $D_{\text{energy}}$ exhibit gradual and steady increase during the loading process, followed by a pronounced upswing in a brief period just prior to specimen failure. The juncture at which the damage parameter experiences a rapid ascent in the curve is termed as the damage parameter mutation point, with all $D_{\text{hit}}$ mutation points occurring earlier than those of $D_{\text{energy}}$. Furthermore, the temporal gap between the appearance of these two mutation points increases with rising temperature. This phenomenon underscores the predictive lag in rock instability when relying on the energy-based damage parameter evolution law compared to AE hit counts. This discrepancy can be attributed to the presence of inherent damage in untreated granite, characterized by internal micro-fractures. During the loading process, these fractures store energy, and with increasing temperature, the quantity and scale of internal granite fractures increase. This accumulation of energy, characterized by low amplitude, is subsequently released only during instances of stress concentration upon damage initiation. Consequently, AE ring counts become active earlier than damage progression.

Leveraging this insightful pattern, the damage parameter mutation point emerges as a valuable precursor indicator of impending rock damage and instability. Moreover, the temporal disparity in the appearance of distinct damage parameter mutation points facilitates early prediction, thereby proving pivotal for the prediction and warning of rock stability in practical engineering applications.

## 4 Conclusions

(1) The influence of temperature on the physical and mechanical properties of granite becomes particularly conspicuous when the heating temperature exceeds 500 °C, resulting in a significant reduction of tensile.

(2) The damage characteristics of granite at varying temperatures are determined through analysis of AE frequency and RA−AF values. Results indicate that with increasing temperature, there is an increase in shear damage modes, augmented crack propagation, and internal damage within the granite.

(3) AE ring counts and cumulative energy provide valuable insights into the dynamic evolution of tensile damage in granite. The size of the fissure formation can be determined by assessing the magnitude of energy and ring count increases. A pronounced increase in both metrics serves as an indicator that rock damage is nearing its threshold, foreshadowing the impending destabilization of the specimen.

(4) The damage parameter curves based on impact counts and energy counts are plotted separately, based on which the damage parameter mutation points are defined. The results show that

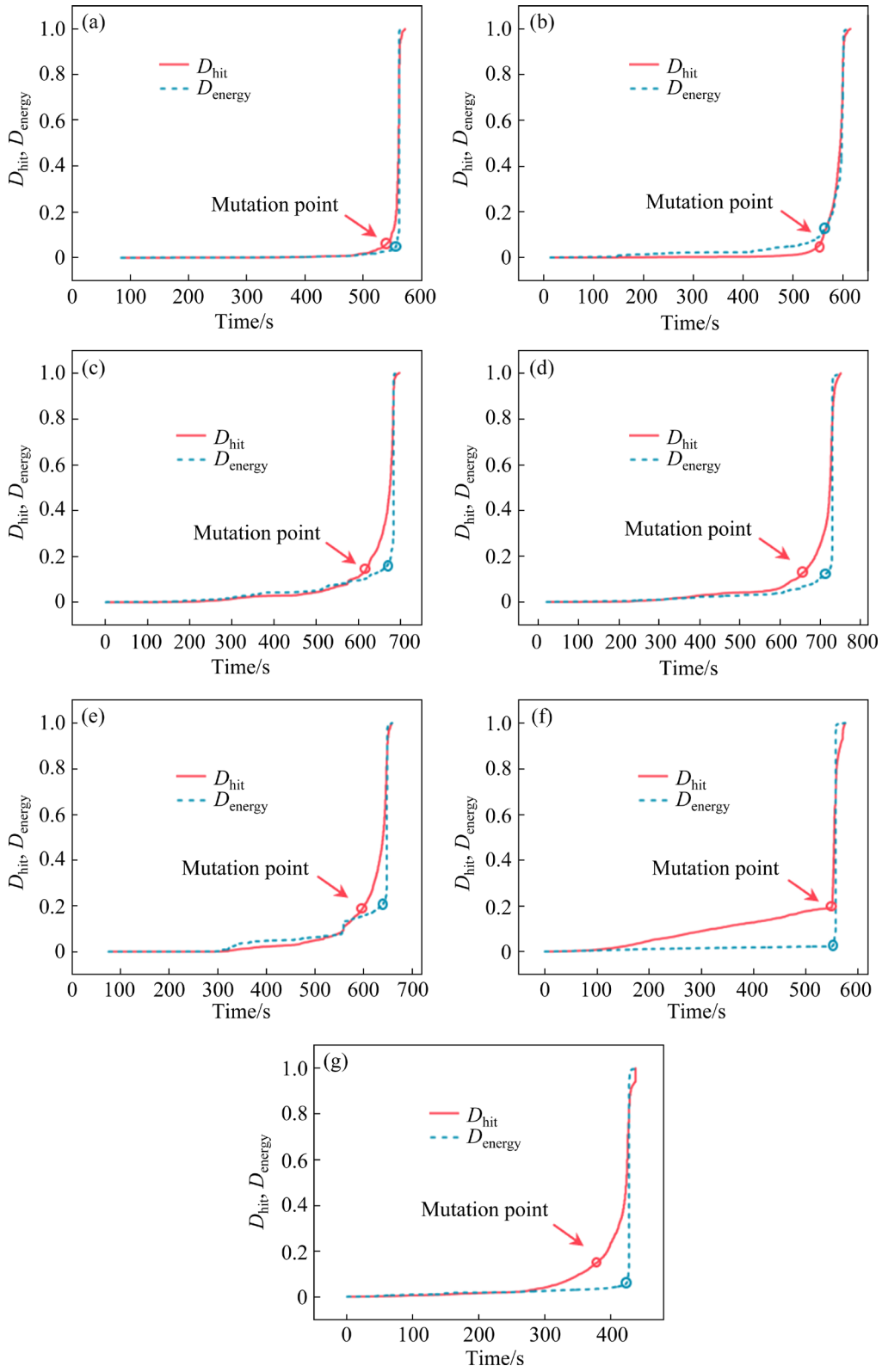


**Fig. 10** Evolution of damage parameters based on AE hit counts and AE energy counts in granite at different temperatures: (a) 50 °C; (b) 100 °C; (c) 200 °C; (d) 300 °C; (e) 400 °C; (f) 500 °C; (g) 600 °C

the mutation points based on hit counts always arrive earlier than that based on energy counts. This suggests that the AE hit counts are significantly active before rock destabilization. The greater the rock damage is, the earlier the mutation points based on impact counts arrive. This temporal discrepancy may be utilized to detect signals indicative of rock destabilization.

## CRediT authorship contribution statement

**Li-chang WANG:** Conceptualization, Writing − Review & editing; **Lu WANG:** Methodology, Software, Data curation, Writing − Original draft; **Meng XU:** Supervision, Conceptualization, Writing − Review & editing; **Wei LONG:** Data curation, Validation.

## Declaration of competing interest

The authors declare that they have no known competing financial interests or personal relationships that could have appeared to influence the work reported in this paper.

## Acknowledgments

This work was financially supported by the Fundamental Research Funds for the Central Universities of Central South University, China (No. CX20220225), the National Natural Science Foundation of China (No. 52104112), the Natural Science Foundation of Hunan Province, China (Nos. 2023JJ20062, 2023JJ30661), the Research Foundation of Department of Natural Resources of Hunan Province, China (No. 20230101DZ), and the Science and Technology Innovation Program of Hunan Province, China (No. 2023RC3051).

## References

[1] WANG Shao-feng, SUN Li-cheng, HUANG Lin-qi, LI Xi-bing, SHI Ying, YAO Jin-rui, DU Shao-lun. Non-explosive mining and waste utilization for achieving green mining in underground hard rock mine in China [J]. Transactions of Nonferrous Metals Society of China, 2019, 29: 1914−1928.

[2] ZHOU X P, CHENG H, FENG Y F. An experimental study of crack coalescence behaviour in rock-like materials containing multiple flaws under uniaxial compression [J]. Rock Mechanics and Rock Engineering, 2014, 47: 1961−1986.

[3] ZHOU X P, LIAN Y J, WONG L N Y, BERTO F. Understanding the fracture behavior of brittle and ductile multi-flawed rocks by uniaxial loading by digital image correlation [J]. Engineering Fracture Mechanics, 2018, 199: 438−460.

[4] ZHOU Xiao-ping, ZHANG Jian-zhi, YANG Sheng-qi, BERTO F. Compression-induced crack initiation and growth in flawed rocks: A review [J]. Fatigue & Fracture of Engineering Materials & Structures, 2021, 44: 1681−1707.

[5] XIE He-ping, LI Cong, HE Zhi-qiang, LI Cun-bao, LU Yi-qiang, ZHANG Ru, GAO Ming-zhong, GAO Feng. Experimental study on rock mechanical behavior retaining the in situ geological conditions at different depths [J]. International Journal of Rock Mechanics and Mining Sciences, 2021, 138: 104548.

[6] HUANG Lin-qi, WANG Jun, MOMENI A, WANG Shao-feng. Spalling fracture mechanism of granite subjected to dynamic tensile loading [J]. Transactions of Nonferrous Metals Society of China, 2021, 31: 2116−2127.

[7] SHU Rong-hua, YIN Tu-bing, LI Xi-bing, YIN Zhi-qiang, TANG Li-zhong. Effect of thermal treatment on energy dissipation of granite under cyclic impact loading [J]. Transactions of Nonferrous Metals Society of China, 2019, 29: 385−396.

[8] ZHOU Xiao-ping, LI Guo-qing, MA Hai-chun. Real-time experiment investigations on the coupled thermomechanical and cracking behaviors in granite containing three pre-existing fissures [J]. Engineering Fracture Mechanics, 2020, 224: 106797.

[9] ZHOU Xiao-ping, FU Liang, CHENG Hao, BERTO F. Cracking behaviours of rock-like materials containing three preexisting flaws after high-temperature treatments [J]. Fatigue & Fracture of Engineering Materials & Structures, 2021, 44: 622−635.

[10] YU Bao-ping, WU Yang-chun, WANG Shuai, XIONG Gui-ming, ZHAO Yang-sheng. Experimental study on mechanical properties of granite taken from Gonghe basin, Qinghai province after high temperature thermal damage [J]. Chinese Journal of Rock Mechanics and Engineering, 2020, 39: 69−83. (in Chinese)

[11] SHA Song, RONG Guan, TAN Jie, HE Ren-hui, LI Bo-wen. Tensile strength and brittleness of sandstone and granite after high-temperature treatment: A review [J]. Arabian Journal of Geosciences, 2020, 13: 598.

[12] GAO Yan-nan, WANG Yun-long, LU Tai-ping, LI Liu-zhou, WU Jin-wen, ZHANG Ze-tian. An experimental study on the mechanical properties of high-temperature granite under natural cooling and water cooling [J]. Advances in Materials Science and Engineering, 2021, 2021: 9018462.

[13] WU Yun, LI Xiao-zhao, HUANG Zhen, WANG Ying-chao, DENG Long-chuan. Effect of thermal damage on tensile strength and microstructure of granite: A case study of Beishan, China [J]. Geomechanics and Geophysics for Geo-Energy and Geo-Resources, 2021, 7: 82.

[14] ZHAO Ya-yong, WEI Kai, ZHOU Jia-qing, LI Xing, CHEN Yi-feng. Laboratory study and micromechanical analysis of mechanical behaviors of three thermally damaged rocks [J]. Chinese Journal of Rock Mechanics and Engineering, 2017, 36(1): 142−151. (in Chinese)

[15] YIN Tu-bin, SHU Rong-hua, LI Xi-bing, WANG Pin, DONG Long-jun. Combined effects of temperature and axial pressure on dynamic mechanical properties of granite [J]. Transactions of Nonferrous Metals Society of China, 2016, 26: 2209−2219.

[16] LIANG Ming, ZHANG Shao-he, SHU Biao. Effect of different cooling ways on Brazilian tension characteristics of heat-treated granite [J]. Journal of Water Resources & Water Engineering, 2018, 29(2): 186−193. (in Chinese)

[17] SI Xue-feng, HUANG Lin-qi, LI Xi-bing, GONG Feng-qiang, LIU Xi-ling. Mechanical properties and rockburst proneness of phyllite under uniaxial compression [J]. Transactions of Nonferrous Metals Society of China, 2021, 31: 3862−3878.

[18] LI Shi-jie, YANG Dao-xue, HUANG Zhen, GU Qi-xong,

ZHAO Kui. Acoustic emission characteristics and failure mode analysis of rock failure under complex stress state [J]. Theoretical and Applied Fracture Mechanics, 2022, 122: 103666.

[19] DONG Long-jun, TAO Qing, HU Qing-chun. Influence of temperature on acoustic emission source location accuracy in underground structure [J]. Transactions of Nonferrous Metals Society of China, 2021, 31: 2468−2478.

[20] DONG Long-jun, LI Xi-bing, ZHOU Zi-long, CHEN Guang-hui, MA Ju. Three-dimensional analytical solution of acoustic emission source location for cuboid monitoring network without pre-measured wave velocity [J]. Transactions of Nonferrous Metals Society of China, 2015, 25: 293−302.

[21] LIU Xi-ling, LIU Zhou, LI Xi-bing, GONG Feng-qiang, DU Kun. Experimental study on the effect of strain rate on rock acoustic emission characteristics [J]. International Journal of Rock Mechanics and Mining Sciences, 2020, 133: 104420.

[22] ZHANG Zheng-hu, MA Ke, LI Hua, HE Zhi-liang. Microscopic investigation of rock direct tensile failure based on statistical analysis of acoustic emission waveforms [J]. Rock Mechanics and Rock Engineering, 2022, 55: 2445−2458.

[23] LIU Han-xiang, JING Hong-wen, YIN Qian, ZHAO Zhen-long, MENG Yao-yao, ZHANG Liang. Study on mechanical properties and fracture behavior of granite after thermal treatment under Brazilian splitting test [J]. KSCE Journal of Civil Engineering, 2023, 27: 643−656.

[24] RODRÍGUEZ P, CELESTINO T B. Application of acoustic emission monitoring and signal analysis to the qualitative and quantitative characterization of the fracturing process in rocks [J]. Engineering Fracture Mechanics, 2019, 210: 54−69.

[25] XIE He-ping, PENG Rui-dong, JU Yang. Energy dissipation of rock deformation and fracture [J]. Chinese Journal of Rock Mechanics and Engineering, 2004, 23: 3565−3570. (in Chinese)

[26] ZHANG Yan-bo, WU Wen-rui, YAO Xu-long, LIANG Peng, SUN Lin, LIU Xiang-xin. Study on spectrum characteristics and clustering of acoustic emission signals from rock fracture [J]. Circuits, Systems, and Signal Processing, 2020, 39: 1133−1145.

[27] WANG Ping, YIN Tu-bing, LI Xi-bing, KONIETZKY H. Dynamic compressive strength and failure mechanisms of microwave damaged sandstone subjected to intermediate loading rate [J]. Transactions of Nonferrous Metals Society of China, 2022, 32: 3714−3730.

[28] YIN Tu-bing, SHU Rong-hua, LI Xi-bing, WANG Pin, LIU Xi-ling. Comparison of mechanical properties in high temperature and thermal treatment granite [J]. Transactions of Nonferrous Metals Society of China, 2016, 26: 1926−1937.

[29] MAHANTA B, SINGH T N, RANJITH P G. Influence of thermal treatment on mode I fracture toughness of certain Indian rocks [J]. Engineering Geology, 2016, 210: 103−114.

[30] ZHOU Xiao-ping, ZHANG Jiang-zhi, QIAN Qi-hu, NIU Yong. Experimental investigation of progressive cracking processes in granite under uniaxial loading using digital imaging and AE techniques [J]. Journal of Structural Geology, 2019, 126: 129−145.

[31] WANG Rui, SUN Chen-ke, DENG Xiang-hui, WANG Yun-cai, LONG Kai. Damage evolution of phyllite based on uniaxial compression and acoustic emission tests [J]. Arabian Journal of Geosciences, 2021, 14: 1958.

[32] ZHOU Xiao-ping, ZHANG Jiang-zhi. Damage progression and acoustic emission in brittle failure of granite and sandstone [J]. International Journal of Rock Mechanics and Mining Sciences, 2021, 143: 104789.

[33] MUÑOZ-IBÁÑEZ A, DELGADO-MARTÍN J, HERBÓN-PENABAD M, ALVARELLOS-IGLESIAS J. Acoustic emission monitoring of mode I fracture toughness tests on sandstone rocks [J]. Journal of Petroleum Science and Engineering, 2021, 205: 108906.

[34] ZHANG Zheng-hu, DENG Jian-hui, ZHU Jian-bo, LI Lin-hui. An experimental investigation of the failure mechanisms of jointed and intact marble under compression based on quantitative analysis of acoustic emission waveforms [J]. Rock Mechanics and Rock Engineering, 2018, 51: 2299−2307.

[35] ZHOU Xiao-ping, WANG Yun-teng, ZHANG Jian-zhi, LIU Fei-nan. Fracturing behavior study of three-flawed specimens by uniaxial compression and 3D digital image correlation: Sensitivity to brittleness [J]. Rock Mechanics and Rock Engineering, 2019, 52: 691−718.

[36] DONG Long-jun, ZHANG Yi-han, MA Ju. Micro-crack mechanism in the fracture evolution of saturated granite and enlightenment to the precursors of instability [J]. Sensors, 2020, 20: E4595.

[37] CARPINTERI A, CORRADO M, LACIDOGNA G. Heterogeneous materials in compression: Correlations between absorbed, released and acoustic emission energies [J]. Engineering Failure Analysis, 2013, 33: 236−250.

[38] ZHANG He, CHEN Qing-lin, WANG Xiao-jun, ZHAO Kui, ZENG Qiang. Acoustic emission parameter characterization of damage process of the limestone with different rockburst tendencies [J]. Minerals, 2022, 12: 1423.

[39] ZHAO Kang, SONG Yu-feng, YAN Ya-jing, GU Shui-jie, WANG Jun-qiang, GUO Xiao, LUO Cai-jun, SUO Tian-yuan. Mechanics and acoustic emission fractal characteristics of surrounding rock of tantalum–niobium mine under splitting condition [J]. Natural Resources Research, 2022, 31: 149−162.

[40] PAN Ji-liang, WU Xu, GUO Qi-feng, XI Xun, CAI Mei-feng. Uniaxial experimental study of the deformation behavior and energy evolution of conjugate jointed rock based on AE and DIC methods [J]. Advances in Civil Engineering, 2020, 2020: 8850250.

[41] WU Chen, GONG Feng-qiang, LUO Yong. A new quantitative method to identify the crack damage stress of rock using AE detection parameters [J]. Bulletin of Engineering Geology and the Environment, 2021, 80: 519−531.

[42] ZHANG Jiang-zhi, ZHOU Xiao-ping. AE event rate characteristics of flawed granite: from damage stress to ultimate failure [J]. Geophysical Journal International, 2020, 222: 795−814.

[43] SUN Bing, YANG Hao-wei, ZENG Sheng, LOU Yu. Damage constitutive and failure prediction of artificial

single-joint sandstone based on acoustic emission [J]. Geotechnical and Geological Engineering, 2022, 40: 5577−5591.
[44] YANG T H, LI L C, THAM L G, TANG C A. Micromechanical model for simulating the hydraulic fractures of rock[C]// Computational Methods 2006. Dordrecht: Springer Netherlands, 2006: 1835−1840.
[45] ZHANG Zhao-peng, ZHANG Ru, XIE He-ping, LIU Jian-feng, WERE P. Differences in the acoustic emission characteristics of rock salt compared with granite and marble during the damage evolution process [J]. Environmental Earth Sciences, 2015, 73: 6987−6999.

# 花岗岩在不同温度劈裂载荷下的损伤演化与失稳前兆

王李昌[1,2]，王 璐[1,2]，徐 蒙[1,2]，隆 威[1,2]

1. 中南大学 地球科学与信息物理学院，长沙 410083；
2. 中南大学 有色金属成矿预测与地质环境监测教育部重点实验室，长沙 410083

**摘 要：**为了阐明深地钻探中花岗岩在劈裂载荷与高温作用下的复杂机械和损伤特性，对经 50~600 ℃处理的花岗岩试样进行巴西劈裂声发射(AE)试验。结果表明，温度变化会使花岗岩的机械与声发射特性发生改变，从而改变其破裂演化过程。当温度超过 500 ℃时，花岗岩的抗拉强度大幅降低，剪切损伤模式占比增加。此外，破裂速率亦呈现明显增长趋势。在基于撞击数和能量计数的损伤参数演化曲线的基础上，定义“损伤参数突变点”来判断作为岩石破坏的前兆信息。基于撞击数的“突变点”比岩石失稳的信号提前到达，且岩石损伤越大，提前的时间越久。通过这个时间差，可以达到预警岩石失稳的效果。

**关键词：**深地钻探；岩石损伤；声发射；高温；劈裂荷载

**(Edited by Xiang-qun LI)**